JGR Planets

RESEARCH ARTICLE
10.1029/2019JE005985

Special Section:
Studies of the 2018/Mars Year 34 Planet-Encircling Dust Storm

Effects of the MY34/2018 Global Dust Storm as Measured by MSL REMS in Gale Crater

D. Viúdez-Moreiras[1], C. E. Newman[2], M. de la Torre[3], G. Martínez[4], S. Guzewich[5], M. Lemmon[6], J. Pla-García[1], M. D. Smith[5], A.-M. Harri[7], M. Genzer[7], A. Vicente-Retortillo[4], A. Lepinette[1], J. A. Rodriguez-Manfredi[1], A. R. Vasavada[3], and J. Gómez-Elvira[1]

[1]Centro de Astrobiología (CSIC-INTA) and Spanish National Institute for Aerospace Technology (INTA), Madrid, Spain, [2]Aeolis Research, Pasadena, CA, USA, [3]Jet Propulsion Laboratory, California Institute of Technology, Pasadena, CA, USA, [4]University of Michigan, Ann Arbor, MI, USA, [5]NASA Goddard Spaceflight Center, Greenbelt, MD, USA, [6]Space Science Institute, College Station, TX, USA, [7]Space Research and Observation Technologies, Finnish Meteorological Institute, Helsinki, Finland

Key Points:
- Atmospheric opacity over Gale Crater was increased by more than 8 times and disturbed all the atmospheric variables measured by REMS
- REMS data suggest that the nighttime near-surface atmosphere stability was reduced and its water abundance increased during the GDS
- The semidiurnal mode peaked after the local opacity maximum, suggesting different dust abundance inside and outside Gale

Supporting Information:
- Supporting Information S1
- Data Set S1

Correspondence to:
D. Viúdez-Moreiras,
viudezmd@inta.es

Citation:
Viúdez-Moreiras, D., Newman, C. E., de la Torre, M., Martínez, G., Guzewich, S., Lemmon, M., et al. (2019). Effects of the MY34/2018 global dust storm as measured by MSL REMS in Gale crater. *Journal of Geophysical Research: Planets*, *124*, 1899–1912. https://doi.org/10.1029/2019JE005985

Received 29 MAR 2019
Accepted 19 JUN 2019
Accepted article online 1 JUL 2019
Published online 22 JUL 2019

Abstract The Rover Environmental Monitoring Station (REMS) instrument is on board NASA's Mars Science Laboratory (MSL) Curiosity rover. REMS has been measuring surface pressure, air, and ground brightness temperature, relative humidity, and ultraviolet (UV) irradiance since MSL's landing in 2012. In Mars Year (MY) 34 (2018) a global dust storm reached Gale Crater at L_s ~ 190°. REMS offers a unique opportunity to better understand the impact of a global dust storm on local environmental conditions, which complements previous observations by the Viking landers and Mars Exploration Rovers. All atmospheric variables measured by REMS are strongly affected albeit at different times. During the onset phase, the daily maximum UV radiation decreased by 90% between sols 2075 (opacity ~1) and 2085 (opacity ~8.5). The diurnal range in ground and air temperatures decreased by 35 and 56 K, respectively, with also a diurnal-average decrease of ~2 and 4 K respectively. The maximum relative humidity, which occurs right before sunrise, decreased to below 5%, compared with prestorm values of up to 29%, due to the warmer air temperatures at night, while the inferred water vapor abundance suggests an increase during the storm. Between sols 2085 and 2130, the typical nighttime stable inversion layer was absent near the surface as ground temperatures remained warmer than near-surface air temperatures. Finally, the frequency domain behavior of the diurnal pressure cycle shows a strong increase in the strength of the semidiurnal and terdiurnal modes peaking after the local opacity maximum, also suggesting differences in the dust abundance inside and outside Gale.

1. Introduction

The Martian dust cycle greatly impacts atmospheric and surface temperatures and hence the circulation, since the atmospheric dust abundance and distribution strongly affects the solar and thermal radiation absorbed and scattered in the atmosphere and hence also the radiation received at the surface (e.g., Hassler et al., 2014 and references therein; Leovy & Zurek, 1979; Madeleine et al., 2011). The role of dust in the modern climate and weather of Mars therefore also has major implications for the design and safety of future human missions.

Local and regional dust storms are ubiquitous on Mars, particularly between areocentric solar longitudes (L_s) 180–360° (Table 2 of Zurek & Martin, 1993; Figure 2 in Wang & Richardson, 2015). Every few Mars years, however, regional storms grow and merge to become a global dust storm (GDS), which is generally defined as a storm whose associated dust haze expands to cover all longitudes over the majority of both hemispheres. Wind-driven dust lifting is a necessary mechanism for injecting dust into the Martian atmosphere during GDS onset (e.g., Basu et al., 2004; Kahre et al., 2006 and references therein; Newman et al., 2002b; Ryan & Henry, 1979; Tillman, 1988), due to the very strong local-to-global scale positive feedbacks associated with this mechanism for lifting dust (Newman et al., 2002a). However, due to the rarity of such events, the evolution of the near-surface atmospheric thermal state and circulation during the onset, expansion/mature, and decay phases of a GDS has rarely been studied at the surface (e.g., Tillman, 1988; Zurek, 1982).

Although the Rover Environmental Monitoring Station (REMS) on the Mars Science Laboratory (MSL) Curiosity rover (Gómez-Elvira et al., 2012; Gómez- Elvira et al., 2014) did not have a working wind sensor

during the MY34 GDS, it was able to measure surface pressure, air and ground brightness temperature, relative humidity, and ultraviolet (UV) irradiance in six spectral bands, for a total of between 9 and 15 hr per sol (including at least 5 min of monitoring every hour) at a frequency of 1 Hz (Gómez-Elvira et al., 2012; Gómez- Elvira et al., 2014). These atmospheric variables reveal how the atmospheric thermal balance and large-scale structure were affected and may also be compared to numerical model simulations to help understand how the atmospheric circulation and near-surface winds were likely impacted at each stage of the storm.

The previous GDS occurred in 2007 and was observed by several spacecraft from orbit: Mars Reconnaissance Orbiter, Mars Odyssey, and Mars Express (Fedorova et al., 2018; Guzewich et al., 2017; Smith, 2009; Wang & Richardson, 2015). However, only the Mars Exploration Rovers (MER) were at that moment on the surface, and although able to measure the evolving optical depth (Lemmon et al., 2015) they were not equipped with the sensors needed to study the dust storm's impact on the near-surface environment. Only the Viking Lander 1 and 2 spacecraft in the 1970s measured some of the aforementioned variables from the surface during the two GDS that developed in MY12 (1977) at L_s ~ 204° (Ryan & Henry, 1979) and at L_s ~ 275° (Ryan & Sharmann, 1981; Tillman, 1988; Zurek & Martin, 1993). In May 2018, after 5 Mars years without a GDS, orbiters observed precursor storms that grew until becoming global in mid-June. The effects of this MY34 GDS reached Gale Crater in early June, when the atmospheric opacity increased by a factor of 8 in comparison to typical values for this season, reaching an optical depth of ~8.5 at 880 nm (Guzewich et al., 2019). MSL instruments were able to measure the onset, expansion/maturation, and decay phases of this storm in unprecedented detail, from inside a crater, including providing the first measurements of how relative humidity and UV irradiation in different spectral bands varied during the GDS.

This manuscript is structured as follows: Section 2 briefly describes the REMS instrument. Section 3 describes the Gale Crater atmospheric environment and presents the effects of the GDS on the crater meteorology from a diurnal-average perspective. Section 4 focuses on the diurnal cycles observed during the storm, and their comparison to the nominal cycles for the same season. Finally, section 5 presents the paper's conclusions.

2. The REMS Instrument

The REMS instrument (Gómez-Elvira et al., 2012) is a suite of six environmental sensors: pressure, air temperature, ground surface brightness temperature (hereafter referred to as ground temperature), relative humidity (RH), wind, and UV radiation. REMS is composed of four units spread throughout the rover. Two units are located on booms attached to the rover's Remote Sensing Mast, with wind and air temperature sensors on both booms, a relative humidity sensor on one boom, and a ground temperature sensor on the other. The UV sensor unit is placed on the rover deck. The pressure sensor is located inside the rover body and connected to the outside by a small tube, which has a high efficiency particulate air filter to minimize the accumulation of dust inside the sensor, the tube, and for planetary protection purposes.

REMS measures for the first 5 min each Local Mean Standard Time hour by default (where an hour is defined as 1/24th of a Mars sol and a minute as 1/60th of an hour), plus typically 7 complete hours per sol, which are added according to a predefined cadence designed to, for example, monitor the time of peak insolation every sol, the sunrise period in many sols, and cover a complete diurnal cycle with 1-Hz measurements every 6 sols (Gómez- Elvira et al., 2014; Newman et al., 2017). During the GDS, however, this cadence was increased to cover a complete diurnal cycle every 3 sols, in order to better monitor the impact of the storm (Guzewich et al., 2019). All REMS sensors have been fully functional since landing, except for the Wind Sensor that was damaged during MSL's landing and remained only partially functional until sol 1491 (over the southern spring equinox in MY33), when its active board was damaged, possibly by saltating particles raised by the strong winds as the rover sat in the Bagnold Dune Field (Viúdez-Moreiras et al., 2019a, 2019b).

The UV sensor is exposed to dust deposition that attenuates the photodiodes signal, hence UV signals must be corrected in order to obtain the absolute irradiance. The correction can be performed by cross correlating the 1-Hz UV sensor observations with radiance measurements made by the Mastcam camera, which takes measurements far less frequently (Smith et al., 2016; Vicente-Retortillo et al., 2018). The net result of the GDS was to significantly enhance dust deposition on the REMS UV sensors, as was seen by comparing

Figure 1. Dust deposition on the ultraviolet sensor: comparison between Mars Science Laboratory sols 2036 (prestorm) and 2216 (after the storm), taken by Mars Hand Lens Imager. The images were taken at different times of sol, hence with different sun position, as evidenced by the different sun glint locations at the edges of the photodiodes. It can be seen in the zooms for both images of the same photodiode that the sensor is almost blocked by the dust, which highlights the deposition of dust over the rover due to the dust storm.

images taken by the Mars Hand Lens Imager (MAHLI) just prior to (MSL sol 2036) and just after (sol 2216) the GDS (see Figure 1).

3. Gale Crater Environment and General Effects of the Global Dust Storm

3.1. Phases of the GDS in Gale Crater

The chronology of the 2018/MY34 GDS is shown in Table 1. For a global perspective of its origin, expansion/mature and decay phases, see, for example, Guzewich et al. (2019). Precursor dust storms originated in the northern hemisphere across Acidalia and Utopia Planitia at $L_s \sim 180°$, expanding and merging with others along the receding southern seasonal CO_2 polar cap. Effects of the storm first reached Gale at $L_s \sim 190°$ (sol 2075), with Mastcam 880-nm opacity increasing from ~0.7 to ~1.5 by sol 2080. The steepest opacity increase occurred between $L_s = 192.5$ and 195.5° (sols 2080–2085), when it reached a peak value of ~8.5. After this, opacity declined until it returned to climatological values at $L_s \sim 245°$ (sol 2157). Compared to previous reported GDSs 15–20 sol expansion is comparable but slower than the 1977A storm (Pollack et al., 1979; Zurek, 1982) and among the slowest decay at 85 sols from its peak, comparable to another early storm in MY25/2001 (Cantor, 2007; Wang & Richardson, 2015).

The atmospheric variables reacted at different times to the GDS; in particular, pressure appeared to react first to the GDS. However, air and ground temperatures, and pressure, differed the most from climatological

Table 1
Sequence of Events Related to the MY34/2018 Global Dust Storm, Focused on Gale Crater

Event	Date	L_s (deg)	MSL sol
Precursor storms across Acidalia and Utopia Planitia	May 2018	~180	~2060
Expansion/Maturation phase (expansion and merging of regional storms)	Early June	~180–190	2060–2075
Storm reaches Gale (start of the onset phase at Gale)[a]	Early June	~190	2075
Period of largest increase at Gale	Mid-June	~192.5–195	2080–2084
Peak at Gale	Mid July	~195	2085
Highly dusty phase at Gale	Mid July	~195–203	2085–2100
Decay phase[b]	Mid September	~203–250	2101–~2169

[a]Note that the *onset* phase at Gale is defined as the onset of changes observed inside Gale Crater, which occurs ~15 sols after onset of the global dust storm. [b]Decay phase based on the atmospheric variables measured by Rover Environmental Monitoring Station. The local 880-nm opacity, measured by Mastcam, showed a decrease starting 16 sols earlier at sol 2085.

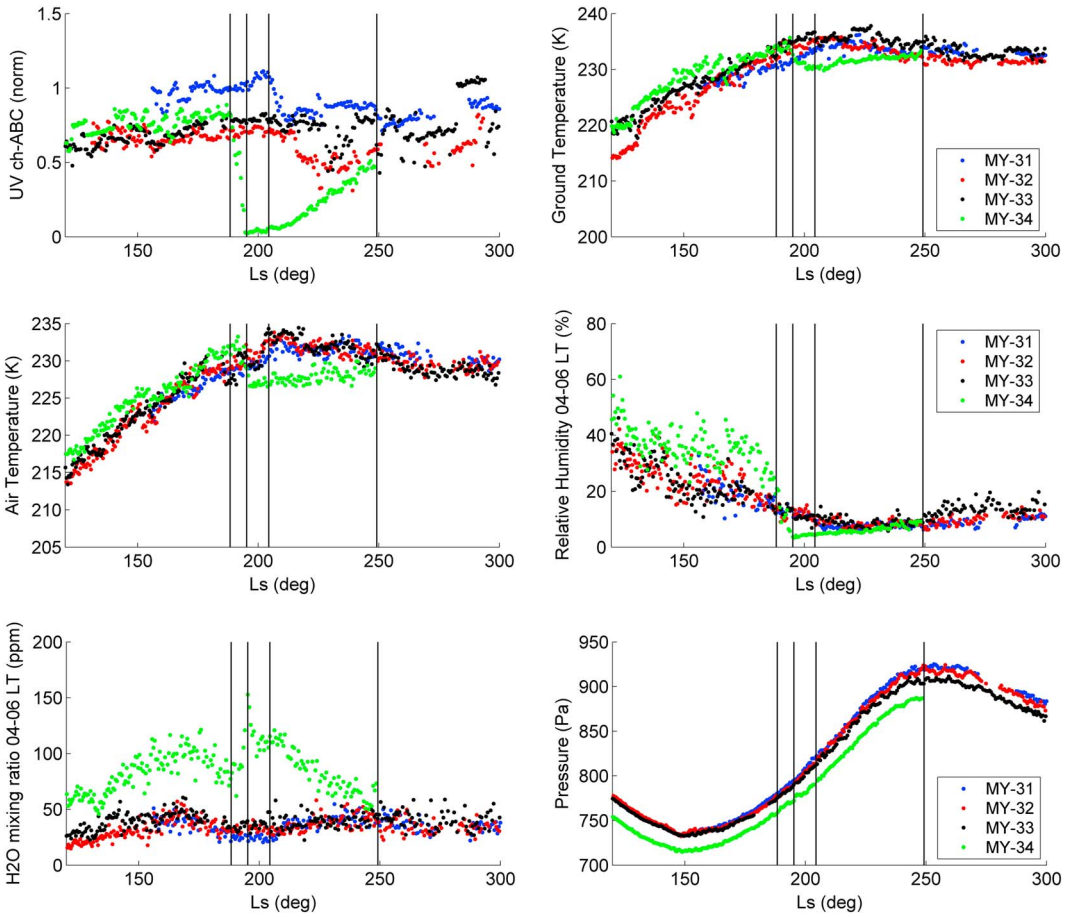

Figure 2. Interannual comparison of the intraseasonal (L_s = 120–300°) evolution as a function of solar longitude (MY color coded) of (a) normalized values of the daily maximum ultraviolet UV flux measured by the ABC channel, (b) daily mean ground temperature, (c) daily mean near-surface air temperature, (d) daily maximum relative humidity (generally achieved between 04:00 and 06:00 Local True Solar Time, LTST), (e) water vapor volume mixing ratio inferred at the same time as the relative humidity shown in (d), and (f) daily mean atmospheric pressure. Vertical lines show the start times of the global dust storm onset (sol 2075), highly dusty (sol 2085), and decay (sol 2100) phases in Gale Crater, as well as the end of the decay phase (sol 2169), as defined in Table 1.

values between sols ~2085 and 2100. For our investigation, we define this period as the "highly dusty phase." Between sols 2101 and ~2169, these variables gradually returned to the normal climatological conditions for this season, hence we define this as the "decay phase." Note that the local opacity (as measured by Mastcam and the REMS UV sensors) in fact began to decrease at the start of the highly dusty phase as defined here, but we define the storm's phases in Gale with respect to the local atmospheric response rather than dust loading.

3.2. Dust Storm Onset and Highly Dusty Phases

Figure 2 overlays REMS measurements obtained for the four observed Martian years as a function of areocentric solar longitude, since landing at L_s ~ 150° in MY31 until L_s ~ 300° in MY34. The interannual comparison between seasonal periods shown here (between L_s = 120° and 300°) encompasses the onset (sols 2075–2084), highly dusty (sols 2085–2100), and decay phases of the GDS during MY34 as observed in Gale Crater, and comparison with previous years at the same L_s demonstrates the magnitude of the dust storm effects in the REMS measurements. Figure 3 shows the evolution, over the details of the whole GDS period (sols 2060–2170) only for MY34, of (i) the daily mean, maximum and minimum pressure, air temperature, and ground temperature; (ii) relative humidity and water vapor abundance averaged over roughly the coldest period of each sol; and (iii) UV irradiance. A summary of the numerical values is presented in Tables 2 and 3.

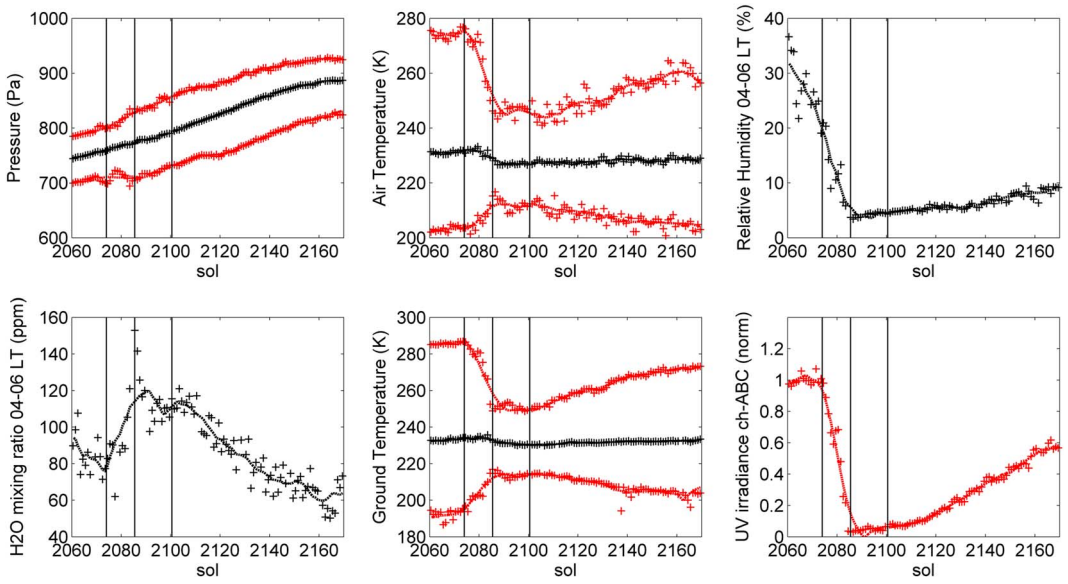

Figure 3. Evolution of REMS variables (sols 2060–2170) for the period encompassing the onset (sols 2075–2084), highly dusty (sols 2085–2100), and decay phases of the GDS. Daily mean, maximum, and minimum values are shown for pressure (a) and temperatures (b and e), while the relative humidity (c) and water mixing ratio (d) values correspond to values where the relative humidity reaches its maximum (between 4:00 and 6:00 LTST) and their uncertainty is lower. Finally, the daily maximum ultraviolet (UV) irradiance (f) is shown normalized to the value on sol 2070. A 20-sol mobile average is also shown for each variable for a better visualization. As in Figure 2, vertical lines show the start times of the GDS onset (sol 2075), highly dusty (sol 2085), and decay (sol 2100) phases in Gale Crater.

Among all measurements, the most dramatic effect was seen in the surface radiative environment (Figures 2a and 3f), with ~95% measured attenuation in UV fluxes in the REMS UV-ABC channel, which ranges from 200 to 380 nm, between L_s ~ 190° and 195.5° (sols 2075–2085), as a result of the rise in the amount of suspended dust. Such a decrease is consistent with a relative reduction in the daily surface insolation from ~75% to ~3.5% as compared to that at the top of the atmosphere (TOA) and with a reduction in the contribution of direct radiation to the total daily insolation at the surface from ~50% to less than 0.1% of its value at the TOA (Vicente-Retortillo et al., 2015). Note that UV fluxes have been normalized to values at the beginning of MSL mission in Figure 2 and to values at sol 2070 in Figure 3. The values have not been corrected for inaccuracies in the angular response of the UV sensors and dust deposition (Smith et al., 2016; Vicente-Retortillo et al., 2018).

The abrupt decrease in surface solar radiation between L_s ~ 190° and 195.5° only caused a moderate decrease in the daily mean surface (Figures 2b and 3e) and air (Figures 2c and 3b) temperatures. The diurnal-average air temperature was ~231 K prior to the dust storm but fell by only ~4 to ~227 K during the highly dusty phase (Table 2). The impact on the diurnal range of air temperatures was far more dramatic, however, with the diurnal range, $T_{rng} = T_{max} - T_{min}$, decreasing from ~71 to ~36 K (T_{rng} ~ 35 K) between the start of the onset and highly dusty phases. This behavior was also observed in the 1977A and 1977B GDSs (Ryan & Henry, 1979; Ryan & Sharmann, 1981; Tillman, 1984), both at Viking 1 (VL1) and Viking 2 (VL2) landing sites (22.5°N–48°W and 48°N–230°W, respectively). Also, this range is close to the 35 K reported by VL1 during the 1977A storm by Ryan and Henry (1979). Maximum temperatures decreased from ~276 to ~249 K, and minimum temperatures increased from ~202 to ~209 K over the same period (Table 3), as atmospheric opacity increased rapidly. The physics behind this are discussed in detail in section 4.2. Similar to air temperature, the diurnal-average ground temperature decreased by only ~2 K (from a prestorm value of ~233 K) due to the GDS but showed a far bigger change in the diurnal range, $Tg_{rng} = Tg_{max} - Tg_{min}$, which decreased from ~94 to ~38 K (Tg_{rng} ~ 56 K) during the onset phase of the storm. The maximum ground temperature decreased from ~286 to ~249 K, while the minimum increased from ~187 to ~211 K. Also observed is a slight decrease in T_{max}, and Tg_{max}, and an increase in T_{min} and Tg_{min}, at the end of the highly dusty phase, which is consistent with the observed increase in MastCam opacity (see section 4.2).

Table 2
Comparison of Sets of 10 Sols During the Nominal (sols 2060–2070) and Highly Dusty (Sols 2090–2100) Atmosphere Periods in Selected REMS Variables

	Nominal atmosphere		Dusty atmosphere		Differences	
Variable	Mean	SEM	Mean	SEM	Absolute	Relative
Pressure (Pa)	750	1.14	784	1.48	34.6	5%
Air temperature (K)	231	0.158	227	0.110	−3.96	−2%
Ground temperature (K)	233	0.158	231	0.155	−2.15	−1%
Relative humidity (%)[a]	28.9	1.71	4.46	$5.05{\cdot}10^{-2}$	−24.4	−85%
H_2O mixing ratio (ppm)[b]	86.2	3.70	107	1.86	21.3	25%
UV irradiance ch-ABC (norm)	1.00	9.19×10^{-3}	4.89×10^{-2}	2.00×10^{-3}	−0.951	−95%

Note. The mean and the standard error of the measurements (SEM) are shown for each variable. REMS = Rover Environmental Monitoring Station; UV = ultraviolet.
[a]Measured between 04:00 and 06:00 LTST. [b]Inferred from relative humidity, temperature and pressure, and averaged between 04:00 and 06:00 LTST.

The daily maximum RH measured by REMS, which typically occurs between 4:00 and 6:00 LTST when air temperature is the lowest (Harri et al., 2014; Savijärvi et al., 2016, 2019a), is shown in Figures 2d and 3c. The daily maximum RH abruptly decreased from ~29% prior to the dust storm to less than 5% during the highly dusty phase (between L_s = 190° and 195°), returning to climatological values of ~10% at L_s ~ 250° as the storm abated. As this measurement is highly influenced by the air temperature, it is better to look at the inferred water vapor volume mixing ratio (VMR) when considering how the actual atmospheric water abundance changed. This may be calculated using contemporaneous REMS measurements of RH, air temperature, and atmospheric pressure, and is shown in Figures 2e and 3d. Prior to the storm, between L_s = 170° and 190°, VMR values showed a decreasing trend (as in previous years; Harri et al., 2014; Martín-Torres et al., 2015; McConnochie et al., 2018; Savijärvi et al., 2015). We note that the significantly larger VMR (and slightly larger RH) values in MY 34 compared to all prior years started to occur at L_s ~ 60° (not shown), well before the dust storm reached Gale, which might be due to differences in the local circulation and properties of the terrain (thermal inertia and porosity, Savijärvi et al., 2019b) as the rover ascended Aeolis Mons.

Even taking into account the interannual variability prior to the onset phase (Figure 2), a strong increase in VMR was seen during the onset phase until sol 2085, from mean values of ~86 ppm (although with high variability in the range 70–95 ppm) to values exceeding 150 ppm. Between sols 2085 and 2090, however, the water abundance decreased again to ~107 ppmv, meaning that the water abundance peaked at the same time as the dust opacity over Gale. Although it could be the result of global effects, previous global dust storms observed from orbit suggest lower water abundances during a global dust storm (e.g., Fedorova et al., 2018, and reference therein). The increase in the nighttime near-surface water abundance observed by MSL REMS could be the result of reduced water adsorption by the regolith at night, due to the warmer nighttime temperatures, resulting in an increase in the atmospheric water vapor (Viúdez-Moreiras et al., 2018), and is consistent with previous studies suggesting this process for exchanging water between the regolith and the atmosphere (e.g., Savijärvi et al., 2015, 2016). In addition, the disappearance of the typical inversion in the near-surface layer during the highly dusty phase and the first sols of the decay phase (see section 4.2) may also increase the water vapor mixing ratio by means of enhanced vertical mixing. Both processes acting together could drive the observed water abundance

Table 3
As Table 2 But for Diurnal Maximum, Minimum, and Mean Amplitudes Within the Nominal (Sols 2060–2070) and Highly Dusty (sols 2090–2100) Atmospheres

	Nominal atmosphere			Dusty atmosphere		
Variable	Maximum	Minimum	Amplitude	Maximum	Minimum	Amplitude
Pressure (Pa)	795	699	84.4	858	713	124
Air temperature (K)	276	202	70.7	249	209	36.3
Ground temperature (K)	286	187	93.6	254	211	38.0

Note. This table is focused on pressure, air and ground temperatures.

during the GDS. The impact of the GDS on daytime or diurnal averaged water abundance cannot be determined, due to the very low daytime relative humidity being smaller than the sensor uncertainties. Similarly, the low predawn relative humidity values after sol 2085 result in more uncertain VMR values; therefore, the values of the reported VMRs during the highly dusty phase should be considered with a high error bar (e.g., Harri et al., 2014).

Figure 2f illustrates the interannual changes in daily mean atmospheric pressures measured by REMS. The lower mean pressures in MY34 compared to MYs 31–33 are due to the rover's higher elevation on the slopes of Aeolis Mons after the rover began climbing more rapidly than before. Focusing on the period surrounding the GDS, however, the mean pressure varies according to the usual seasonal cycle due to the sublimation of the Martian polar caps and was barely affected by the storm. However, the diurnal pressure amplitude range, $p_{\mathrm{rng}} = p_{\mathrm{max}} - p_{\mathrm{min}}$, within each sol varies during the storm, which was also observed during the 1977A and 1977B dust storms (Ryan & Henry, 1979; Ryan & Sharmann, 1981). The diurnal range increased from ~84 Pa prior to the storm to ~124 Pa on average during sols 2090–2100. This is due in part to the impact of the dust storm on thermal tides and in part to the storm's impact on mean air temperatures during the day and night, as described further in section 4.

3.3. Dust Storm Decay Phase

The pressure returned to the nominal diurnal cycle around sol 2170 (Figure 3a), with slight differences in accordance with the seasonal evolution (Guzewich et al., 2016; Haberle et al., 2014). The daily pressure amplitude also decreased from the average amplitude within the highly dusty phase of ~124 to ~103 Pa, close to its nominal values for this season.

The diurnal-average air temperature was apparently constant at ~227 K during the decay phase (Figure 3). However, this is the result of two independent processes taking place at the same time. On the one hand, REMS data for previous years show the air temperature achieved its maximum values in Gale at L_s ~ 210° (Figure 2), just after the start of the decay phase when a warming trend is typical. On the other hand, the presence of dust produced a decrease in the diurnal-average near-surface temperature (a rapid decrease of ~4 K occurred during the onset phase), but this dust was slowly disappearing during the decay phase. Both competing processes acting simultaneously resulted in roughly constant air temperatures during the decay phase. A similar behavior is observed in the ground temperature. Over the decay phase, the diurnal range in both air and ground temperature that abruptly decreased during the onset phase was also gradually restored.

The relative humidity also returned to nominal values (Figure 3), which were ~8–10% in previous years for this season (Figure 2). However, the water vapor mixing ratio was also apparently reduced to ~60 ppm, lower than the values observed during the onset of the GDS (Table 2) and quite close to the levels observed during previous years for this season by REMS (Figure 2), which significantly contrast to the higher values observed during the current Martian year. This suggests that the prestorm increase in water vapor abundance in MY34 compared to prior years, which was previously ascribed to the rover's higher position on the slopes of Aeolis Mons, may also have a seasonal component. Thus, changes in transport of water vapor into and out of Gale Crater in different seasons could be the responsible. In addition, differences in the nighttime temperatures between MY34 and previous years may play a role in the observed variability. It would also be possible that the dust deposited on surface during the fall out of the dust storm could contribute to a change in the properties of the near-surface terrain, becoming closer to similar years.

Finally, all UV channels measured by REMS experienced a significant but slower increase in irradiance over the decay phase as a result of the decrease in the dust optical depth. Figure 3f shows irradiances normalized to those values on sol 2070, just prior to the onset phase, and demonstrates that the UV ABC-channel increased its signal from <10% (during the highly dusty phase) to ~60% of the values measured prior to onset. These irradiances are in fact only slightly below typical values for this time of year (see Figure 2), and given that Mastcam reported typical seasonal values by this point, it is likely that the increase in dust deposition on the sensor photodiodes during the storm (Figure 1) attenuated the UV signal in its aftermath, rather than higher-than-normal atmospheric dust loading continuing to exist.

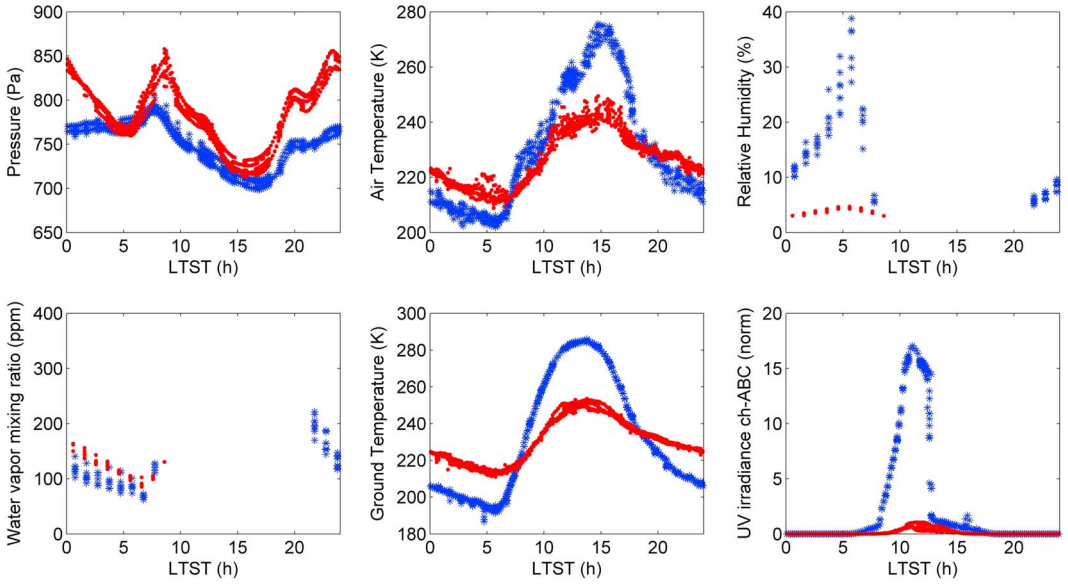

Figure 4. Comparison between the *nominal* diurnal cycle (blue asterisks) just prior to storm onset (sols 2060–2070) and the *highly dusty* diurnal cycle (red dots) within the highly dusty phase of the global dust storm (sols 2085–2095). The values for very low relative humidity (<3%) are considered unreliable and therefore are not shown (see text). Note that the ultraviolet radiance after noon in the nominal case is strongly affected by shadows in all sols; that is, the direct component of the sunlight is fully or partially blocked by the rover's remote sensing mast during the ~12:00–14:00 period.

4. Effects of the Dust Storm on the Diurnal Cycle

This section presents the effect of the GDS on the diurnal cycles of meteorological variables observed by REMS. Figure 4 shows the diurnal cycle for pressure, air and ground brightness temperature, relative humidity, and the normalized irradiance of the UV-ABC channel, both before the GDS (sols 2060–2070) and during its highly dusty phase (sols 2085–2095). Figure 5 complements Figure 4 by showing the evolution of the ground-to-air temperature difference and the diurnal pressure modes over the prestorm to poststorm period.

4.1. Pressure Diurnal Cycle

The nominal and highly dusty diurnal pressure cycles are shown in Figure 4a. The main contributors are the global thermal tides. Tides are driven by the solar cycle and modulated by the presence of water ice clouds (Kleinböhl et al., 2013), topography, and surface albedo and thermal inertia, in addition to dust loading, which largely determines the amplitude of the thermal tide signature (Hess et al., 1977; Leovy & Zurek, 1979; Wilson & Hamilton, 1996; Zurek, 1980). Atmospheric dust is directly connected to atmospheric heating, which produces expansion and motion of air masses, which in turn drives surface pressure changes. The tidal signature on Mars is typically dominated by the diurnal mode in relatively clear conditions and by the semidiurnal mode in highly dusty conditions (Hess et al., 1977; Guzewich et al., 2016; Leovy & Zurek, 1979; Lewis & Barker, 2005; Rafkin et al., 2016; Wilson & Hamilton, 1996; Zurek, 1980). This is due to the longer vertical wavelength of the latter mode, which makes it more responsive to the more vertically extended heating produced by increased atmospheric absorption of solar radiation (by dust particles) during a major dust storm (Leovy & Zurek, 1979; Lewis & Baker, 2005; Zurek, 1980). Before interpreting the daily pressure mode observed by MSL, it should be highlighted that it is not possible to separate the signal of the migrating diurnal thermal tide from the nonmigrating nearly resonant Kelvin wave (Guzewich et al., 2016; Zurek, 1976; Zurek & Leovy, 1981), westward and eastward propagating, respectively, resulting in a destructive interference. Also, in Gale Crater, nontidal contributions such as hydrostatic adjustment flows that are a result of day-night contrasts in solar heating and hence background atmospheric temperatures over regions of topography possibly amplify the diurnal amplitude (Richardson & Newman, 2018). As the air column expands during a period of heating, the surface pressure decreases everywhere above some level along a slope but increases everywhere below that level along the slope, in order to maintain an along-slope hydrostatic balance. This process, which involves transfer of air down the slope, reverses at night when the air columns

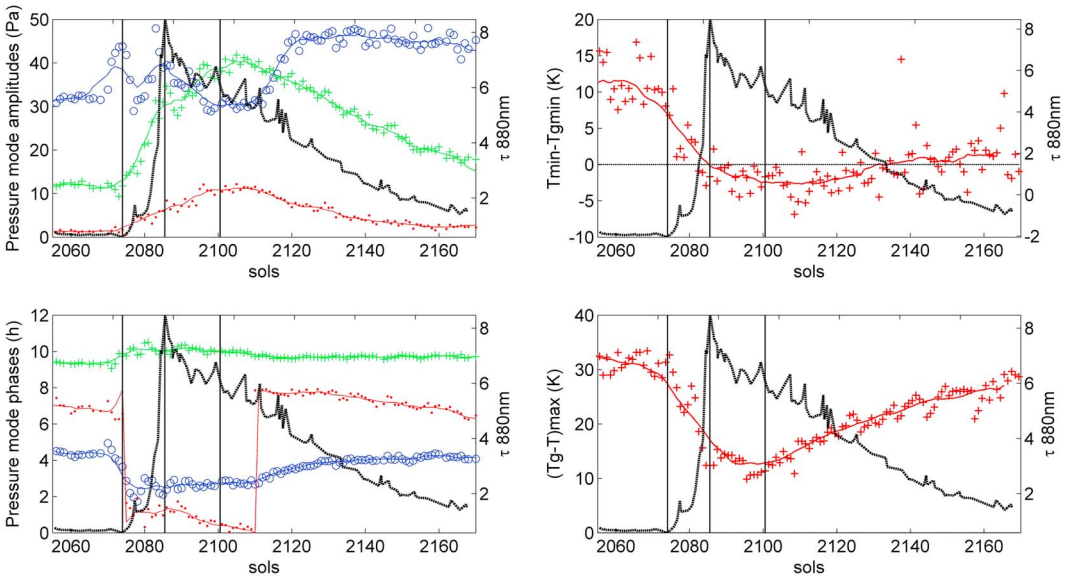

Figure 5. (top left): Evolution of the diurnal pressure tide amplitude (blue circles), compared to the semidiurnal (green crosses) and the terdiurnal (red points) tide amplitudes; (bottom left): as in the top left but for the diurnal pressure tide phases; (top right): difference between minimum surface and air temperatures (i.e., the difference at night) at 1.5 m above the surface; (bottom right): difference between maximum surface and air temperatures. Moving average values are also shown for a better visualization of the trend. Mastcam opacity is included in every plot (black lines) for comparative purposes. The first vertical line indicates the onset of global dust storm effects in Gale, the second indicates the start of the *highly dusty* phase, and the third indicates the start of the decay phase, from the Rover Environmental Monitoring Station variables perspective.

contract and air must be transferred up the slope to again maintain the along-slope surface pressure distribution in hydrostatic balance.

Figure 4a shows a clear increase in the daily signal's amplitude during the dust storm, with a far clearer two-peak structure, due to the increase in the semidiurnal pressure mode. Figure 5 shows the first three pressure modes (diurnal, semidiurnal and terdiurnal) for sols 2060–2170, encompassing the onset, highly dusty, and decay phases of the GDS in Gale Crater. The diurnal pressure amplitude first reacted ~4 sols before the arrival of dust to the crater (sol 2075) and showed considerable variability during the onset phase (~30–45 Pa), including rapid increases and decreases of more than 10 Pa in a few sols. However, the diurnal pressure amplitude then steadily decreased over the highly dusty phase, to below prestorm levels (~30 Pa), before recovering and increasing again during the decay phase of the storm, eventually stabilizing at ~45 Pa after another ~20 sols. By contrast, the semidiurnal pressure tide amplitude increased rapidly throughout the onset and highly dusty phases, exceeding the diurnal amplitude for half of the highly dusty phase and over half of the decay phase. The semidiurnal tide phase showed an increase before the arrival of dust to Gale Crater (sol 2075) and peaked roughly in sol 2080, recovering the nominal values well after the start of the decay phase, with an oscillatory behavior around the general trend. The diurnal pressure phase, which generally ranged from 4 to 5 hr during MY31 to MY33 (see Guzewich et al., 2016 for MY31–MY32), also reacted before sol 2075 and fell to values less than 2 hr between sols 2075 and 2080, which was never previously observed over the entire mission, showing also a slow recovering trend.

Given that the diurnal and semidiurnal tidal modes have different vertical wavelengths, the different times at which their amplitudes peaked is likely related to changes in the regional and global dust distribution as the storm evolved. The diurnal tide amplitude is more dependent on the local, regional and tropical dust abundance, while the semidiurnal mode depends to a greater extent on regional and globally averaged dust abundance, due to the predominance of the gravest Hough mode in the migrating semidiurnal tide (Chapman & Lindzen, 1970; Guzewich et al., 2016). The transitory amplitude and phase disturbances in the diurnal pressure mode before sol 2075, and during the GDS, could be allocated to the enhancement of the nonmigrating Kelvin wave, as a result of longitudinal asymmetries in the atmospheric dust content. A

similar behavior was found during the 1977B dust storm based on tidal analysis of Vikings data (Zurek & Leovy, 1981) and posterior general circulation model simulations (Wilson & Hamilton, 1996). Also, the deep decrease observed in the diurnal amplitude during the GDS could be partly due to a reduction of the nontidal hydrostatic flow contribution. As discussed in Guzewich et al. (2019), the ~50% reduction in diurnal air temperature range during the GDS would reduce this nontidal contribution by a similar amount, from a contribution of ~15 Pa before the storm to ~8 Pa during it. The evolution of the terdiurnal mode, negligible under *nominal* conditions and usually enhanced around the solstices when hemispheric thermal gradients are greater, contributed significantly to the daily amplitude of pressure in the *highly dusty* phase and followed the same evolution as the semidiurnal mode. It could be the result of hemispheric differences in atmospheric dust content during the GDS.

Overall, the pressure tides began to respond to the storm well before Mastcam opacity showed any significant increase. However, the peak in semidiurnal and terdiurnal tide amplitudes—and the dip in diurnal tide amplitude—occurred about 20 sols after the peak in Mastcam opacity. Given that Mastcam optical depth measurements are *local* measurements inside Gale and that the pressure tides respond to the larger-scale atmospheric dust abundance, the offsets in timing of the pressure tides response and Mastcam opacity suggest different dust abundances inside the crater versus the regional-to-global dust distribution. In fact, Thermal Emission Imaging System (THEMIS) observations (Smith, 2009) suggest that the optical depth peak for this storm in tropical latitudes was over L_s ~ 200–205° (M. Smith, personal communication, 2019), corresponding to MSL sols ~2095–2100, much later than the peak inside Gale Crater (sol 2085, corresponding to L_s ~ 195°). Similarly, from the Mars Climate Sounder (MCS; Kass et al., 2018; Kleinböhl et al., 2017; McCleese et al., 2007), the peak of the dust abundance was at L_s ~ 201° in the southern tropics (D. Kass, personal communication, 2019). This is the same time as the peak for the entire tropics; however, the value remained close to the maximum until L_s ~209°. In the southern midlatitudes, MCS data suggest that the dust column opacity peak was not reached until L_s ~ 209° (D. Kass, personal communication, 2019). This is in agreement with the peak in the amplitude of the semidiurnal mode at Gale, inferred from the REMS pressure data, at sol ~2105 (L_s ~ 205°). Orbiter data thus seem to confirm that opacities continue to rise in the general tropical atmosphere during the GDS even as they fall inside the crater. This is in contrast to the good correlation between tidal amplitudes and local optical depth measurements observed in nominal atmospheric conditions, which indicate that the atmospheric opacities at Gale Crater are normally largely representative of the global average (Guzewich et al., 2016). Interpreting these results further, including the secondary effects of different dust vertical profiles and optical properties during the storm as well as the influence of nonmigrating tides in the observed pressure tides, would require dedicated modelling work.

4.2. Air and Ground Temperature Diurnal Cycles

As briefly described in section 3, the GDS resulted in an overall decrease in the amplitude of the diurnal air and ground temperature cycles: overnight minimum temperatures increase and daytime maximum temperatures decrease, phenomena also observed in Ryan and Henry (1979) and modeled by Wilson and Richardson (2000) during the Vikings GDS(s). Both daily ranges followed closely the temporal evolution of the growth and decay in Mastcam opacity seen at Gale, unlike the pressure tides which seemed more responsive to the global evolution that predated the arrival of the dust at Gale. Maximum ground temperatures decreased, by about 35 K, only when the increase in local opacity (hence decrease in insolation) occurred over Gale during the growth phase of the GDS, while the minimum ground temperatures increased by some 20 K as a consequence of the more opaque and hence warmer atmospheric layers above the rover preventing more nighttime IR radiative cooling of the surface. Near-surface air temperatures responded similarly (though with a smaller amplitude), reflecting stronger than usual thermal radiative coupling between the surface and opaque atmosphere, while the reduction in insolation reaching the surface resulted in the mean ground and near-surface air temperatures decreasing by ~2 and ~4 K, respectively (Table 2).

It is also interesting to note the change in sign of the surface-to-air temperature difference at the coldest and warmest times of sol (shown in Figure 5). Prior to the storm, the surface cooled faster than the near-surface air after sunset, with upward longwave radiation from the surface exceeding downward longwave radiation from the atmosphere, and the surface became up to 10 K colder at night (Figure 4e). The sensible heat flux was also directed into the surface when the atmosphere was warmer at this time. Midway through the GDS onset phase, however, opacities became sufficiently high that the surface received far more longwave

radiation from the atmospheric layers above it at night than it was emitting itself, and the surface became warmer than the atmosphere again. This means that the usual "nocturnal inversion layer" was absent near the surface between sols ~2085 and ~2130, and hence, the nighttime near-surface atmosphere stability was significantly reduced for more than 40 sols.

During the daytime, the prestorm surface became much warmer than the atmosphere, with little solar radiation being absorbed by the thin, transparent atmosphere and most going into heating the surface, which then heated the atmosphere above it (Figure 5). However, when opacities increased during the GDS onset phase, the insolation reaching the surface was reduced and more was absorbed by the atmosphere. The surface remained warmer than the near-surface air during the day throughout the GDS, but the daytime sensible heat flux was reduced due to the decrease in the thermal gradient between the ground and the air, resulting in no convective vortices exceeding 0.5 Pa or dust devils being detected by MSL between sols 2083 and 2107 (Guzewich et al., 2019).

4.3. Relative Humidity and Atmospheric Water Abundance Diurnal Cycles

As noted in section 3, the relative humidity also experienced great variability between nominal and highly dusty conditions, highly influenced by the air temperatures. This difference is also observed throughout the diurnal cycle. Note that Figures 2 and 3 showed respectively the maximum and mean RH and VMR over only the 04:00–06:00 LTST timeslot, as this contains the highest RH measurements and when the inferred VMRs have the highest reliability. By contrast, Figures 4c and 4d show every RH and inferred VMR over the whole sol. Results for very low RH (<3%) are considered unreliable and therefore are not shown, in accordance to Savijarvi et al. (2015).

For the nominal diurnal cycle, this results in the loss of confidence in the measurements from ~8:00 until ~20:00 LTST, but during the GDS—when higher nighttime temperatures produce lower RH values—measurements from ~20:00 to ~00:00 LTST are also unreliable. The nominal cycles showed very small RH during the daytime, slow growth after sunset, faster growth after midnight, maximum values of almost 40% just prior to sunrise (which occurs at ~6:00 LTST at this time of year), followed by a rapid drop (Savijärvi et al., 2016). During the highly dusty phase, however, RH values remained below 5% throughout the diurnal cycle, although a small maximum still occurred at the same time as usual. Also, the evening period (19:00 – 00:00 LTST), and particularly the first 2 hr (19:00–21:00 LTST) present RH values larger than expected for this diurnal timeslot (Savijärvi et al., 2016; Savijarvi et al., 2019a), perhaps due to an unresolved sensor issue. We do not show the *nominal* values within the 19:00–21:00 LTST diurnal timeslot. Also, the 21:00–00:00 LTST diurnal timeslot should be considered with care. There are no values within 19:00–00:00 LTST for the highly dusty phase (RH < 3%).

By contrast, the VMR had its maximum at some time during the day and decreased from at least 21:00LTST onward (at least in the nominal case), reaching its minimum value shortly after sunrise, while RH was still very high. This is consistent with model analyses of the atmospheric water vapor abundance decreasing as the regolith cools and water is adsorbed into the soil (Savijärvi et al., 2016; Savijarvi et al., 2019a; Steele et al., 2017), with this water then starting to desorb back into the atmosphere when the surface again heats up after sunrise. The overnight atmospheric water abundance during the dusty diurnal cycle seems to be higher than during the nominal cycle, in accordance with the results presented in Table 2. There is some sign that this trend may have reversed a few hours after sunrise—that is, that there is less water vapor in the highly dusty phase—due to the surface temperature first becoming cooler compared to the nominal case, hence the rate of desorption presumably being slower. Unfortunately, while the trends are likely indicative of what is happening, the large uncertainty in the inferred values of water abundance prevents highly reliable values from being calculated for the mixing ratios.

4.4. UV Irradiance Diurnal Cycle

The maximum values for the nominal and dusty diurnal cycles correspond to ~12:00 LTST, corresponding to the smallest solar zenith angles. As stated above, the apparent attenuation observed during the highly dusty phase was 95% (Table 2), although additional dust deposition on the photodiodes (Figure 1) during the storm may also have slightly affected this value. Figure 4f shows a diurnal cycle during the nominal and highly dusty phases, but it is important to note that the afternoon UV irradiance during the nominal phase was

strongly affected by shadows, with the rover mast blocking direct solar radiation for the rover's orientation on those sols.

The effects of shadows seem to disappear during the GDS. This may be because, while most of the irradiance reaching the surface in the nominal cycle corresponds to the direct component, the strong attenuation during the highly dusty phase ($\tau > 8$) implies an almost complete contribution by scattered sunlight.

5. Summary and Conclusions

The MY34/2018 GDS reached Gale in early June 2018 and significantly disturbed the atmospheric parameters measured by MSL REMS. Atmospheric dust increased the Mastcam 880-nm opacity over Gale Crater by more than 8 times in comparison to the typical values for this season, peaking on MSL sol 2085 and largely decaying steadily thereafter. The atmospheric variables reacted at different times to the GDS, with effects first noted in pressure data, particularly in the pressure diurnal tide.

We define a period over which the REMS variables exhibited steady dust storm conditions that were abnormal from climatological conditions (highly dusty phase sols 2085–2100) and another during which the variables gradually returned to the climatological conditions for this season (decay phase sols 2101–~2169).

REMS results show that the daily maximum of the UV radiation decreased by 90% over only 10 sols after the dust storm first reached Gale, as a result of the dust absorption and scattering in the UV band. Diurnal-average air and ground temperatures decreased almost 4 and 2 K due to the lower radiation reaching the surface. In addition, their diurnal cycles and maxima and minima experienced strong disturbances. The daytime cooling and the nighttime warming resulting from the GDS reduced the diurnal amplitude of near-surface air temperature by 35 K (from 71 to 36 K) and of ground temperature by 56 K (from 94 to 38 K). During the highly dusty period, the ground temperature remained warmer than the near-surface air temperature during the nighttime, and therefore the typical nighttime inversion layer was absent near the surface, due to the greater coupling between the surface and atmosphere in the more opaque conditions. Consequently, the nighttime near-surface atmosphere stability was significantly reduced over a period of more than 40 sols, allowing enhanced convection during the nighttime.

The pressure diurnal cycle showed an unusual frequency domain behavior, with enhanced semidiurnal and terdiurnal tidal amplitudes, and first an increase then a decrease in the diurnal tide, as a result of the different response of atmospheric thermal tidal modes to large-scale changes in the vertical and horizontal dust distribution. There was a delay between both the semidiurnal and terdiurnal peaks of the tidal modes observed by REMS (sol ~2105, L_s ~ 205°) and the peak in the dust optical depth observed by Mastcam (sol ~2085, L_s ~ 195°), which suggest different dust abundance during the highly dusty phase inside and outside Gale Crater. Orbital observations made by THEMIS suggest that the optical depth peak for this storm in tropical latitudes corresponds to MSL sol ~2095–2100. In addition, MCS data suggest that the dust column opacity peak is not reached in the southern midlatitudes until L_s ~ 209°, which reinforces this hypothesis.

The maximum of the relative humidity, which occurs right before sunrise, decreased drastically to below 5%, compared with prestorm mean values of 29%, due to the warmer air temperatures at night. The inferred values for water mixing ratio suggest an increase during the highly dusty phase, peaking at sol 2085 (corresponding to the peak in local dust opacity), and also evolve accordingly to the minimum air and ground temperatures. REMS data suggest that an adsorption-desorption mechanism in the regolith is driving the diurnal cycle of the near-surface atmospheric water vapor abundance and that the GDS reduced its strength due to the decrease in the diurnal range of ground temperature. Also, the enhanced vertical mixing suggested to occur during the GDS' nighttime could be favoring the increase in nighttime water vapor abundances in the near-surface layer. However, the large uncertainties in the inferred mixing ratios mean that these results should be considered with care.

The MSL REMS measurements are the most detailed *within* a GDS since Vikings in the 1970s, and they are also the first measurements acquired in a region with significant topography that plays a strong role in the near-surface environment, which differs to those from Vikings on large plain landing sites.

Acknowledgments

All data used here are from the NASA's Planetary Data System (PDS). REMS data are obtained from the MOD data set, except the REMS UV, obtained from the ENV processing level. REMS data, including MOD and ENV levels, are available in the PDS after a 6 months embargo since its acquisition (https://pds.nasa.gov/). The data presented in Figure 5 are included in the supporting information. This research has been partially supported by the Spanish Ministry of Economy and Competiveness (MINECO), under project ESP2016-79612-C3-1-R. The authors thank Richard Zurek and an anonymous reviewer, whose comments helped improve this paper; and David Kass for his valuable comments on the evolution of the GDS based on the MCS orbital data. In addition, we wish to express our gratitude to the NASA Mars Science Laboratory for supporting this investigation.

References

Basu, S., Richardson, M. I., & Wilson, R. J. (2004). Simulation of the Martian dust cycle with the GFDL Mars GCM, *Journal of Geophysical Research*, *109*, E11006, https://doi.org/10.1029/2004JE002243

Cantor, B. A. (2007). MOC observations of the 2001 Mars planet-encircling dust storm. *Icarus*, *186*(1), 60–96. https://doi.org/10.1016/j.icarus.2006.08.019

Chapman, S., & Lindzen, R. S. (1970). *Atmospheric tides*. Norwell, MA: D. Reidel.

Fedorova, A., Bertaux, J.-L., Betsis, D., Montmessin, F., Korablev, O., Maltagliati, L., & Clarke, J. (2018). Water vapor in the middle atmosphere of Mars during the 2007 global dust storm. *Icarus*, *300*, 440–457. https://doi.org/10.1016/j.icarus.2017.09.025

Gómez-Elvira, J., Armiens, C., Carrasco, I., Genzer, M., Gómez, F., Haberle, R., et al. (2014). Curiosity's rover environmental monitoring station: Overview of the first 100 sols. *Journal of Geophysical Research: Planets*, *119*, 1680–1688. https://doi.org/10.1002/2013JE004576

Gómez-Elvira, J., Armiens, C., Castañer, L., Domínguez, M., Genzer, M., Gómez, F., et al. (2012). REMS: The environmental sensor suite for the Mars Science Laboratory rover. *Space Science Reviews*, *170*(1-4), 583–640. https://doi.org/10.1007/s11214-012-9921-1

Guzewich, S. D., Lemmon, M., Smith, C. L., Martínez, G., Vicente-Retortillo, Á., Newman, C. E., et al. (2019). Mars Science Laboratory Observations of the 2018/Mars Year 34 global dust storm. *Geophysical Research Letters*, *46*(1), 71–79. https://doi.org/10.1029/2018GL080839

Guzewich, S. D., Newman, C. E., de la Torre Juarez, M., Wilson, R. J., Lemmon, M., Smith, M. D., et al., & the REMS Science Team and MSL Science Team (2016). Atmospheric tides in Gale Crater, Mars. *Icarus*, *268*, 37–49. https://doi.org/10.1016/j.icarus.2015.12.028

Guzewich, S. D., Toigo, A. D., & Wang, H. (2017). An investigation of dust storms observed with the Mars Color Imager. *Icarus*, *289*, 199–213. https://doi.org/10.1016/j.icarus.2017.02.020

Haberle, R. M., Gómez-Elvira, J., de la Torre Juárez, M., Harri, A. M., Hollingsworth, J. L., Kahanpää, H., et al. (2014). Preliminary interpretation of the REMS pressure data from the first 100 sols of the MSL mission. *Journal of Geophysical Research: Planets*, *119*, 440–453. https://doi.org/10.1002/2013je004488

Harri, A.-M., Genzer, M., Kemppinen, O., Gomez-Elvira, J., Haberle, R., Polkko, J., et al. (2014) Mars Science Laboratory relative humidity observations: Initial results, *Journal of Geophysical Research: Planets*, *119*, 2132–2147. https://doi.org/10.1002/2013JE004514

Hassler, D. M., Zeitlin, C., Wimmer-Schweingruber, R. F., Ehresmann, B., Rafkin, S., Eigenbrode, J. L., et al. (2014). Mars' surface radiation environment measured with the Mars Science Laboratory's Curiosity rover. *Science*, *343*(6169), 1244797. https://doi.org/10.1126/science.1244797

Hess, S. L., Henry, R. M., Leovy, C. B., Ryan, J. A., & Tillman, J. E. (1977). Meteorological results from the surface of Mars: Viking 1 and 2. *Journal of Geophysical Research*, *82*(28), 4559–4574. https://doi.org/10.1029/JS082i028p04559

Kahre, M. A., Murphy, J. R., & Haberle, R. M. (2006) Modeling the Martian dust cycle and surface dust reservoirs with the NASA Ames general circulation model, *Journal of Geophysical Research*, *111*, 0148–0227. https://doi.org/10.1029/2005JE002588

Kass, D., Kleinboehl, A., Shirley, J.H., Schofield, J.T., McCleese, D., & Heavens, N.G. (2018), Overview of the 2018a Global Dust Event from Mars Climate Sounder Observations, presented at the Fall American Geophysical Union Meeting, Washington, DC, December 2018.

Kleinböhl, A., Friedson, A., & Schodield, J. T. (2017). Two-dimensional radiative transfer for the retrieval of limb emission measuremnts in the Mmartian atmosphere. *Journal of Quantitative Spectroscopy & Radiative Transfer*, *187*, 511–522. https://doi.org/10.1016/j.jqsrt.2016.07.009

Kleinböhl, A., Wilson, R. J., Kass, D., Schofield, J. T., & McCleese, D. J. (2013). The semidiurnal tide in the middle atmosphere of Mars. *Geophysical Research Letters*, *40*, 1952–1959. https://doi.org/10.1002/grl.50497

Lemmon, M. T., Wolff, M. J., Bell, J. F. III, Smith, M. D., Cantor, B. A., & Smith, P. H. (2015). Dust aerosol, clouds, and the atmospheric optical depth record over 5 Mars years of the Mars Exploration Rover mission. *Icarus*, *251*, 96–111. https://doi.org/10.1016/j.icarus.2014.03.029

Leovy, C. B., & Zurek, R. W. (1979). Thermal tides and Martian dust storms: Direct evidence for coupling. *Journal of Geophysical Research*, *84*(B6), 2956–2968. https://doi.org/10.1029/JB084iB06p02956

Lewis, S. R., & Barker, P. R. (2005). Atmospheric tides in a Mars general circulation model with data asssimilation, *Advances in Space Research*, *36*, 2162–2168. https://doi.org/10.1016/j.asr.2005.05.122

Madeleine, J.-B., Forget, F., Millour, E., Montabone, L., & Wolff, M. J. (2011). Revisiting the radiative impact of dust on Mars using the LMD Global Climate Model. *Journal of Geophysical Research*, *116*(E11), E11010. https://doi.org/10.1029/2011JE003855

Martín-Torres, F., Zorzano, M. P., Valentín-Serrano, P., Harri, A. M., Genzer, M., Kemppinen, O., et al. (2015). Transient liquid water and water activity at Gale crater on Mars. *Nature Geoscience*, *8*(5), 357–361. https://doi.org/10.1038/ngeo2412

McCleese, D. J., Schofield, J. T., Taylor, F. W., Calcutt, S. B., C, M., Foote, D. M., et al. (2007). Mars Climate Sounder: An investigation of thermal and water vapor structure, dust and condensate distributions in the atmosphere, and energy balance of the polar regions. *Journal of Geophysical Research*, *112*(E5), E05S06. https://doi.org/10.1029/2006JE002790

McConnochie, T. H., Smith, M. D., Wolff, M. J., Bender, S., Lemmon, M., Wiens, R. C., et al. (2018). Retrieval of water vapor column abundance and aerosol properties from ChemCam passive sky spectroscopy. *Icarus*, *307*, 294–326. https://doi.org/10.1016/j.icarus.2017.10.043

Newman, C. E., Gómez-Elvira, J., Marín, M., Navarro, S., Torres, J., Richardson, M. I., et al. (2017). Winds measured by the Rover Environmental Monitoring Station (REMS) during the Mars Science Laboratory (MSL) rover's Bagnold Dunes Campaign and comparison with numerical modeling using MarsWRF. *Icarus*, *291*, 203–231. https://doi.org/10.1016/j.icarus.2016.12.016

Newman, C. E., Lewis, S. R., Read, P. L., & Forget, F. (2002a). Modeling the Martian dust cycle, 1, Representations of dust transport processes. *Journal of Geophysical Research*, *107*(E12), 6-1–6-18. https://doi.org/10.1029/2002JE001910

Newman, C. E., Lewis, S. R., Read, P. L., & Forget, F. (2002b). Modeling the Martian dust cycle, 2, Multiannual radiatively active dust transport simulations. *Journal of Geophysical Research*, *107*(E12), 7-1–7-15. https://doi.org/10.1029/2002JE001920

Pollack, J. B., Colburn, D. S., Flasar, F. M., Kahn, R., Carlston, C. E., & Pidek, D. (1979). Properties and effects of dust particles suspended in the Martian atmosphere. *Journal of Geophysical Research*, *84*(B6), 2929–2945. https://doi.org/10.1029/JB084iB06p02929

Rafkin, S. C., Pla-Garcia, J., Kahre, M., Gomez-Elvira, J., Hamilton, V. E., Marín, M., & Vasavada, A. (2016). The meteorology of Gale Crater as determined from Rover Environmental Monitoring Station observations and numerical modeling. Part II: Interpretation. *Icarus*, *280*, 114–138. https://doi.org/10.1016/j.icarus.2016.01.031

Richardson, M. I., & Newman, C. E. (2018). On the relationship between surface pressure, terrain elevation, and air temperature. Part I: The large diurnal surface pressure range at Gale Crater, Mars and its origin due to lateral hydrostatic adjustment. *Planetary and Space Science*, *164*, 132–157. https://doi.org/10.1016/j.pss.2018.07.003

Ryan, J. A., & Henry, R. M. (1979). Mars atmospheric phenomena during major dust storms, as measured at surface. *Journal of Geophysical Research*, *84*(B6), 2821–2829. https://doi.org/10.1029/JB084iB06p02821

Ryan, J. A., & Sharmann, R. D. (1981). Two major dust storms, One Mars year apart: Comparison from Viking Data. *Journal of Geophysical Research*, *86*(C4), 3247–3254. https://doi.org/10.1029/JC086iC04p03247

Savijärvi, H., Harri, A. M., & Kemppinen, O. (2016). The diurnal water cycle at Curiosity: role of exchange with the regolith. *Icarus*, *265*, 63–69. https://doi.org/10.1016/j.icarus.2015.10.00

Savijärvi, H., Harri, A.-M., & Kemppinen, O. (2015). Mars Science Laboratory diurnal moisture observations and column simulations. *Journal of Geophysical Research: Planets*, *120*, 1011–1021. https://doi.org/10.1002/2014je004732

Savijarvi, H., McConnochie, T. H., Harri, A.-M., & Paton, M. (2019a). Annual and diurnal water vapor cycles at Curiosity from observations and column modeling. *Icarus*, *319*, 485–490. https://doi.org/10.1016/j.icarus.2018.10.008

Savijärvi, H., McConnochie, T. H., Harri, A.-M., & Paton, M. (2019b). Water vapor mixing ratios and air temperatures for the three Martian years from Curiosity. *Icarus*, *326*, 170–175. https://doi.org/10.1016/j.icarus.2019.03.020

Smith, M. D. (2009). THEMIS observations of Mars aerosol optical depth from 2002–2008. *Icarus*, *202*(2), 444–452. https://doi.org/10.1016/j.icarus.2009.03.027

Smith, M. D., Zorzano, M. P., Lemmon, M., Martín-Torres, J., & Mendaza de Cal, T. (2016). Aerosol optical depth as observed by the Mars Science Laboratory REMS UV photodiodes. *Icarus*, *280*, 234–248. https://doi.org/10.1016/j.icarus.2016.07.012

Steele, L. J., Balme, M. R., Lewis, S. R., & Spiga, A. (2017). The water cycle and regolith-atmosphere interaction at Gale carter, Mars. *Icarus*, *289*, 56–79. https://doi.org/10.1016/j.icarus.2017.02.010

Tillman, J. E. (1984). Martian meteorology and dust storms from Viking observations. In C. P. McKay (Ed.), *Proceedings of The Case for Mars II conference, Boulder Colo., July 1984*, *Science and Technology Series* (Vol. 62, pp. 333–342). San Diego, CA: American Astronautical Society.

Tillman, J. E. (1988). Mars global atmospheric oscillations: Annually syncronized, transient normal-mode oscillations and the triggering of global dust storms. *Journal of Geophysical Research*, *93*(D8), 9433–9451. https://doi.org/10.1029/JD093iD08p09433

Vicente-Retortillo, Á., Martínez, G. M., Renno, N., Newman, C. E., Ordonez-Etxeberria, I., Lemmon, M. T., et al. (2018). Seasonal deposition and lifting of dust on Mars as observed by the Curiosity rover. *Scientific Reports*, *8*(1), 17576. https://doi.org/10.1038/s41598-018-35946-8

Vicente-Retortillo, A., Valero, F., Vázquez, L., & Martínez, G. M. (2015). A model to calculate solar radiation fluxes on the Martian surface. *Journal of Space Weather and Space Climate*, *5*, A33. https://doi.org/10.1051/swsc/2015035

Viúdez-Moreiras, D., Gómez-Elvira, J., Martínez, G., Guzewich, S., Newman, C., Pla-García, J., et al. (2018), Effects of the MY34/2018 global dust storm in the Gale Crater environment as measured by REMS, presented at the Fall American Geophysical Union Meeting, Washington, DC, December 2018.

Viúdez-Moreiras, D., Gómez-Elvira, J., Newman, C. E., Navarro, S., Marin, M., Torres, J., de la Torre, M., & the MSL team (2019a). Gale surface wind characterization based on the Mars Science Laboratory REMS dataset. Part I: Wind retrieval and gale's wind speeds and directions. *Icarus*, *319*, 909–925. https://doi.org/10.1016/j.icarus.2018.10.011

Viúdez-Moreiras, D., Gómez-Elvira, J., Newman, C. E., Navarro, S., Marin, M., Torres, J., de la Torre, M., & the MSL team (2019b). Gale surface wind characterization based on the Mars Science Laboratory REMS dataset. Part II: Wind Probability Distributions. *Icarus*, *319*, 645–656. https://doi.org/10.1016/j.icarus.2018.10.010

Wang, H., & Richardson, M. I. (2015). The origin, evolution, and trajectory of large dust storms on Mars during Mars years 24-30 (1999-2011). *Icarus*, *251*, 112–127. https://doi.org/10.1016/j.icarus.2013.10.033

Wilson, R. J., & Hamilton, K. P. (1996). Comprehensive model simulation of thermal tides in the Martian atmosphere. *Journal of the Atmospheric Sciences*, *53*(9), 1290–1326. https://doi.org/10.1175/1520-0469(1996)053<1290:CMSOTT>2.0.CO;2

Wilson, R. J., & Richardson, M. I. (2000). The Martian atmosphere during the Viking mission, I: Infrared measurements of atmospheric temperatures revisited. *Icarus*, *145*(2), 555–579. https://doi.org/10.1006/icar.2000.6378

Zurek, R. W. (1976). Diurnal tide in the Martian atmosphere. *Journal of the Atmospheric Sciences*, *33*(2), 321–337. https://doi.org/10.1175/1520-0469(1976)033<0321:DTITMA>2.0.CO;2

Zurek, R. W. (1980). Surface pressure response to elevated heating sources: Comparison of Earth and Mars. *Journal of the Atmospheric Sciences*, *37*(5), 1132–1136. https://doi.org/10.1175/1520-0469(1980)037<1132:SPRTET>2.0.CO;2

Zurek, R. W. (1982). Martian great dust storms: An update. *Icarus*, *50*(2-3), 288–310. https://doi.org/10.1016/0019-1035(82)90127-0

Zurek, R. W., & Leovy, C. B. (1981). Thermal tides in the dusty Martian atmosphere: A verification of theory. *Science*, *213*(4506), 437–439. https://doi.org/10.1126/science.213.4506.437

Zurek, R. W., & Martin, L. J. (1993). Interannual variability of planet-encircling dust storms on Mars. *Journal of Geophysical Research*, *98*(E2), 3247–3259. https://doi.org/10.1029/92JE02936